AGU Advances

RESEARCH ARTICLE
10.1029/2021AV000636

Tropical Continents Rainier Than Expected From Geometrical Constraints

Cathy Hohenegger[1] and **Bjorn Stevens**[1]

[1]Max Planck Institute for Meteorology, Hamburg, Germany

Key Points:

- A conceptual model of tropical precipitation is derived to understand the tropics-wide partitioning of precipitation between land and ocean
- The size and location of continent constrain the tropical land-to-ocean precipitation ratio to lie between 0.74 and 0.95 with a mean of 0.86
- Observed ratios from six data sets are larger than these values, indicating that land receives more than its fair share of precipitation

Supporting Information:

Supporting Information may be found in the online version of this article.

Correspondence to:

C. Hohenegger,
cathy.hohenegger@mpimet.mpg.de

Citation:

Hohenegger, C., & Stevens, B. (2022). Tropical continents rainier than expected from geometrical constraints. *AGU Advances*, *3*, e2021AV000636. https://doi.org/10.1029/2021AV000636

Received 9 DEC 2021
Accepted 21 MAY 2022

Peer Review The peer review history for this article is available as a PDF in the Supporting Information.

Author Contributions:

Conceptualization: Cathy Hohenegger
Formal analysis: Cathy Hohenegger
Investigation: Cathy Hohenegger
Methodology: Cathy Hohenegger, Bjorn Stevens
Supervision: Cathy Hohenegger, Bjorn Stevens
Writing – original draft: Cathy Hohenegger
Writing – review & editing: Cathy Hohenegger, Bjorn Stevens

Abstract Abundant rainfall over tropical land masses sustains rich ecosystems, a crucial source of biodiversity and sink of carbon. Here, we use two characteristics of the observed tropical precipitation distribution, its distinctive zonal arrangement and its partitioning between land and ocean, to understand whether land conditions the climate to receive more than its fair share of precipitation as set by the land-sea distribution. Our analysis demonstrates that it is not possible to explain the tropics-wide partitioning of precipitation unless one assumes that rain is favored over land. Land receives more than its fair share of precipitation by broadening and letting the tropical rainbelts move more, effectively underpinning a negative feedback between surface water storage and precipitation. In contrast, rain is disfavored over land in climate models. Our findings suggest that the abundance of rainfall that shapes the terrestrial tropical biosphere is more robust to perturbations than models have suggested.

Plain Language Summary Many ecosystems depend on the presence of a land surface exposed to precipitation to exist and prosper. In contrast to the marine biota, though, the terrestrial biosphere cannot directly tap into an unlimited reservoir of water molecules that can be recycled to support life. Yet, observations indicate that it rains in mean 3 mm day^{-1} over tropical land and 3 mm day^{-1} over tropical ocean, giving the surprising impression that precipitation amounts are not altered by the presence of land. Investigating the factors controlling this tropics-wide partitioning of precipitation, we show that geometrical constraints actually would lead to a precipitation ratio of 0.86, not 1.0, if the presence of land would not matter. Comparing this theoretical value to observations, we find that the land receives more than its fair share of precipitation. This happens by broadening and letting the tropical rainbelt moves more over land. By quantifying the strength of the land control on the tropics-wide partitioning of precipitation, we can also deduce that a negative feedback exists between evapotranspiration and precipitation. In contrast, repeating the same analysis with climate models reveals a positive feedback, questioning the ability of climate models to simulate regional tropical precipitation changes.

1. Introduction

The 40-year long precipitation record of the Global Precipitation Climatology Project (GPCP; Adler et al., 2016) indicates that it rains in mean 3 mm day^{-1} over tropical land areas and 3 mm day^{-1} over tropical oceanic areas, giving the impression that precipitation amounts are not altered by the presence of land. This may appear surprising as the land, in contrast to the ocean, cannot tap into an unlimited reservoir of water molecules. Moreover, evidence of alterations of precipitation by the surface characteristics exists: the distinct timing of convective precipitation over land versus ocean (Gray & Jacobson, 1977; Wallace, 1975); the scarcity of lightning over ocean (Bang & Zipser, 2015); or the presence of bigger, stronger and more organized convective towers over land (Bang & Zipser, 2015; Zipser & LeMone, 1980). The land has been advanced as the reason the belt of tropical precipitation resides in the northern hemisphere (Philander et al., 1996; Riehl, 1954) and the monsoons exist (Halley, 1686), although its roles in both cases have been disputed (Bordoni & Schneider, 2008; Frierson et al., 2013; Kang et al., 2008). On the mesoscale, precipitation is enhanced at the boundary between maritime and continental air masses (Rhea, 1966), over islands (Sobel et al., 2011), over mountains (Roe, 2005) and the presence of surface heterogeneities, for example, in soil moisture, can locally reshape the spatial distribution of precipitation (Pielke, 2001; Taylor et al., 2011). Whether ultimately the precipitation amounts are enhanced by the land surface characteristics, especially its soil moisture content, nevertheless remains disputed (Hohenegger et al., 2009; Koster & Coauthors, 2004; Taylor et al., 2013).

Table 1
Observational Data Sets With Their Time Period and Resolution

Data set	Version	Time period	Resolution	References
GPCP	2.3	1979–2020	2.5°	Adler et al. (2016)
PERSIANN-CDR		1983–2019	0.25°	Ashouri et al. (2015)
GPCC	v2018	1988–2014	0.5°	Schneider et al. (2018)
HOAPS	3.2	1988–2014	0.5°	Andersson et al. (2017)
CMORPH	1.0	1998–2017	0.25°	Joyce et al. (2004)
TRMM	7.0	2000–2014	0.25°	Huffman et al. (2016)
IMERG	6.0	2015–2020	0.1°	Huffman et al. (2019)

Note. GPCC is only available over land and HOAPS only over ocean.

In this study, we ask how the presence of land influences the partitioning of tropical precipitation between land and ocean. From this answer, we draw some inferences as to the existence of feedbacks between the state of the land surface and precipitation as well as the stability of the wet tropics over land. While it seems obvious that the location and size of land masses must somehow matter as the climate is not zonally symmetric, what is not obvious is whether the land with its distinctive surface characteristics influences the atmosphere in ways that unduly favors it to collect more than its fair share of precipitation as given by geometrical constraints. We answer this question by taking advantage of two features of the observed distribution of tropical precipitation: its distinctive zonal arrangement, which allows us to conceptualize the precipitation distribution as a rainbelt whose parameters can easily be varied as a function of the land-sea distribution; and the ratio between precipitation averaged over tropical land and over tropical ocean, which we denote $\chi(t)$ with t indexing the month.

2. Considered Data Sets and Climate Models

To investigate the extent to which the land can affect $\chi(t)$, predictions of our conceptual model are compared to observations. Given the uncertainties plaguing the retrieval of precipitation, we consider seven data sets, namely GPCP, PERSIANN-CDR, abbreviated as PERSIANN in the reminder of the text, GPCC, HOAPS, CMORPH, TRMM, and IMERG (see Table 1). As reviewed by Sun et al. (2018), the data sets differ in the instruments and retrieval methods they use, their temporal and spatial coverage as well as their spatial resolution. Even within one data set, retrieval methods may slightly differ between land and ocean. This could cause artificial precipitation contrasts between land and ocean, a further motivation for including as many data sets as possible.

For IMERG, we only consider the time period 2015–2020, the time period the new Global Precipitation Measurement (GPM) satellite constellation has been in operation. The version 6 of the IMERG data set also contains reprocessed precipitation data from the TRMM satellite era (2000–2014). We disregard this period as we observed a discontinuity in the precipitation amounts over ocean between these two periods. Each year after 2015 exhibits a lower mean tropical precipitation than any of the years before, in mean by about 0.2 mm day^{-1}, something that is not seen in other observational data sets. The release notes of IMERG also mention that the start of the GPM calibration shifts the probability distribution function of monthly precipitation rates to lower values (see Figure 7 in Huffman et al. (2020)). For the observational data set labeled GPCCHOAPS in Figure 5, we use GPCC over land and HOAPS over ocean as these two separate data sets are only available over land (GPCC) and over ocean (HOAPS). For all the data sets, the analysis is performed on their native grid with their provided land-sea mask if available. Except if noted otherwise, TRMM is always used to derive the required parameters of our conceptual model.

From other available data sets, we do not include in our analysis CPC Merged Analysis of Precipitation and the rain-gauge corrected version of Global Satellite Mapping of Precipitation. In these two satellite-based data sets, the yearly averages of tropical precipitation over land are smaller than in the rain gauge-based data set of GPCC, whereas rain gauges are thought to provide a lower estimate of precipitation. We also eliminate PERSIANN_CCS which exhibits a very low mean value of tropical precipitation over ocean, around 2.4 mm day^{-1} against at least 3 mm day^{-1} in the other data sets.

The ability of state-of-the-art General Circulation Models to represent $\chi(t)$ and its underlying controls is also investigated. We consider the historical simulations from the CMIP6 intercomparison project and focus on the

Table 2
CMIP6 Models

Model name
BCC-CSM2-MR, BCC-ESM1, CanESM5, CESM2, CESM2-WACCM, CNRM-CM-6-1, CNRM-ESM2-1, GFDL-CM4, GISS-E2-1-G, GISS-E2-1-H HadGEM3-GC31-LL, IPSL-CM6A-LR, MIROC6, MPI-ESM-LR, MRI-ESM2-0, SAM0-UNICON, UKESM1-0-LL, EC-Earth3
ACCESS-CM2, ACCESS-ESM1-5, CAMS-CSM1-0, CESM2-FV2, CESM2-WACCM-FV2, CIESM, CMCC-CM2-HR4, CMCC-CM2-SR5, CMCC-ESM2, CanESM5-CanOE, E3SM-1-0, E3SM-1-1-ECA, E3SM-1-1, FIo-ESM-2-0, IITM-ESM, INM-CM4-8, INM-CM5-0, IPSL-CM5A2-INCA, IPSL-CM6A-LR-INCA, MPI-ESM-1-2-HAM, TaiESM1

Note. First 18 models as employed in Fiedler et al. (2020).

time period 2000–2014, matching the TRMM record. We include the same 18 models as employed in Fiedler et al. (2020) for their assessment of precipitation biases across CMIP phases. We also added 21 further models, which became available later on, even though this does not affect the statistics and our conclusions. The considered models are listed in Table 2. The model outputs are regridded on a T63 grid to compute the multi model mean.

Both for the observations and model simulations, $\chi(t)$ is computed as:

$$\chi(t) = \frac{\langle P(\lambda,\phi,t)\Gamma_\ell(\lambda,\phi)\rangle}{\langle \Gamma_\ell(\lambda,\phi)\rangle} \frac{\langle \Gamma_o(\lambda,\phi)\rangle}{\langle P(\lambda,\phi,t)\Gamma_o(\lambda,\phi)\rangle} \quad (1)$$

with the tropical summation operator $\langle\rangle$ defined by: $\langle..\rangle = \int_{-180°}^{180°}\int_{-30°}^{30°} ..\cos(\phi)\,d\phi\,d\lambda$ with λ longitude and ϕ latitude. $P(\lambda, \phi, t)$ denotes the monthly mean rate of precipitation in mm day^{-1}. $\Gamma_\ell(\lambda, \phi)$ denotes a land mask, being unity when at a given point land exists, meaning the land fraction is larger than 0.5, and zero otherwise (unitless). Accordingly, we have an ocean mask, $\Gamma_o(\lambda, \phi)$, with $\Gamma_o(\lambda, \phi) = 1 - \Gamma_\ell(\lambda, \phi)$.

3. The Surprising Zonality of Tropical Precipitation

In the tropics, the precipitation falls in well-defined, zonally extended bands (Figure 1a), a fact recognized in the widespread use of the term "rainbelt" to designate tropical rainfall. But the rains fall in an even more perfect belt than a simple rendering of the long-term mean rainfall, as shown in Figure 1a, would suggest. To show

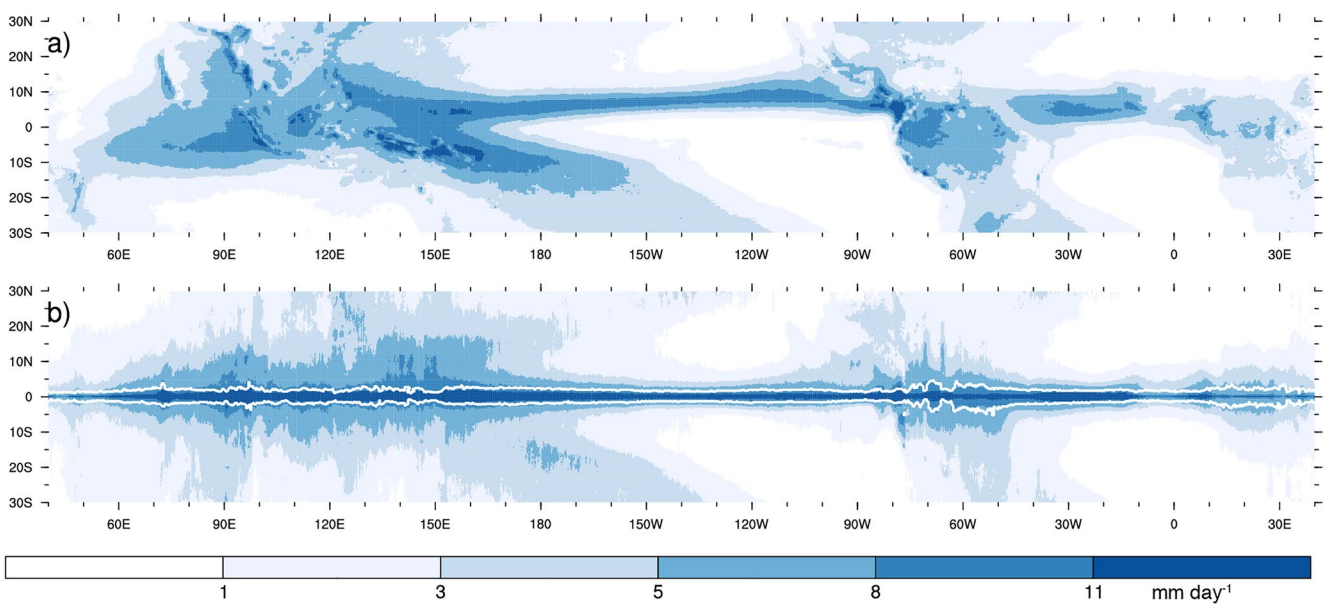

Figure 1. Mean precipitation from TRMM: (a) observed and (b) obtained by shifting each longitude of precipitation meridionally so that the location of its maximum (hydrological equator) lies at 0°N. The shifted precipitation distributions are computed for every month and then averaged. The white isoline indicates where precipitation amounts to 50% of the temporally averaged maxima.

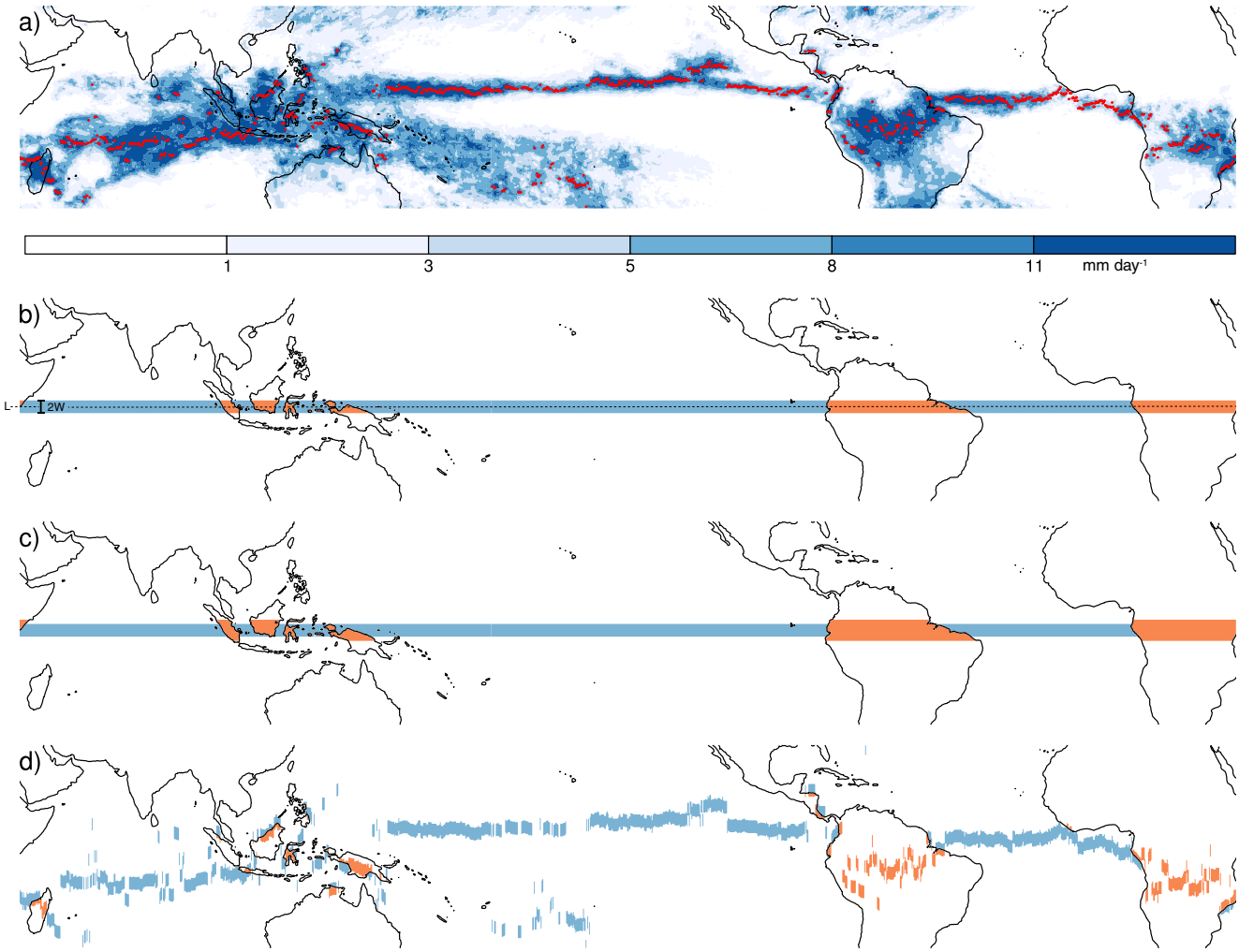

Figure 2. (a) Monthly mean precipitation from TRMM for January 2001 with red markers for the hydrological equators, and corresponding illustration of the rainbelt model for the case with (b) uniform rainbelt (U_RB), (c) asymmetric width (aW_RB), and (d) asymmetric location (aL_RB). Orange for points belonging to the land and blue to the ocean. The definition of the rainbelt location $L(\lambda, t)$ and half-width $W(\lambda, t)$ is illustrated in panel (b). In this rendering, the case of asymmetric intensity (aI_RB) would look like U_RB but the intensity over land (orange points) and ocean (blue points) would be different.

this, we define the hydrological equator to be the latitude of the maximum of the monthly mean precipitation at each longitude and month. The hydrological equator is visualized by the red dots in Figures 2a and 3a for two example months. We then plot the distribution of rainfall relative to the hydrological equator (Figure 1b). The shifting offsets the well-known seasonal migration of the rains that blurs the belt structure in a rendering of the long-term mean. The new rendering reveals the true zonality of the rainbelts, with the presence of one single and noteworthy narrow rainbelt in the long-term mean. Outside a band of $\pm 1.9°$ around the hydrological equator, precipitation intensities already fall to less than half of their maximum. This indicates that one clear precipitation maximum indeed generally exists at each longitude for a given month. Moreover, the uncovered rainbelt exhibits surprisingly little zonal variations in intensity and width, with the imprint of land masses being less easily recognizable.

This property of the precipitation climatology motivates its interpretation using a simple conceptual "rainbelt" model. In this conceptualization, the precipitation falls in one single, zonally continuous belt of half-width $W(\lambda, t)$, intensity $I(\lambda, t)$ and latitudinal location $L(\lambda, t)$. This conceptualization is visualized in Figures 2 and 3 for particular configurations of our rainbelt model, configurations that are explained in the next sections. The intersection between the rainbelt and the underlying land-sea mask $\Gamma(\lambda, \phi)$ provides theoretical values of the expected

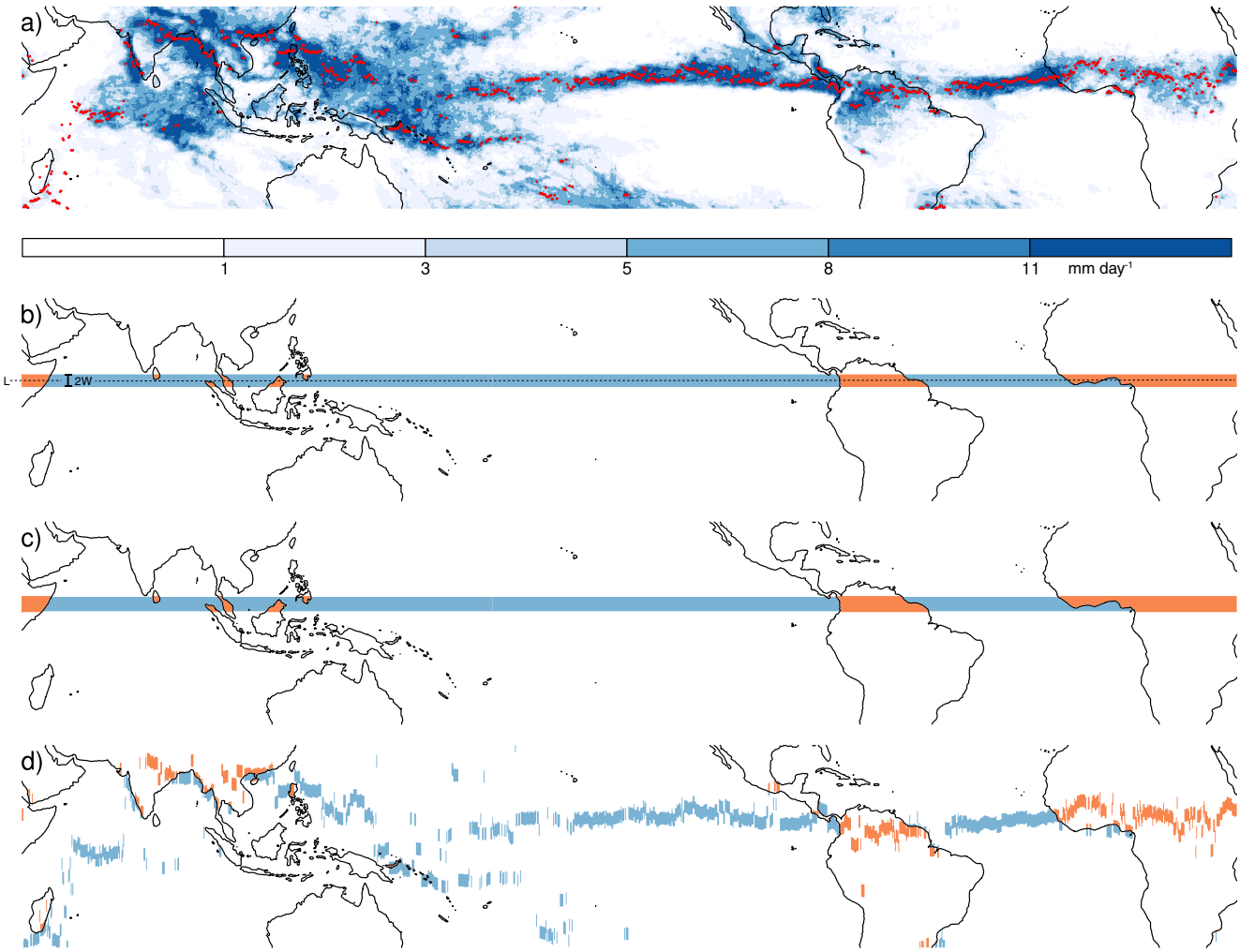

Figure 3. Same as Figure 2 but for July 2001.

tropics-wide partitioning of precipitation $\chi(t)$. These estimates can be contrasted with observed values of $\chi(t)$ to understand the underlying controls on $\chi(t)$.

4. Land Receives More Than Its Fair Share of Precipitation

We start by investigating the null hypothesis that the land receives its fair share of precipitation as set by geometrical constraints. If the land did not statistically influence the distribution of precipitation, the parameters of the rainbelt model would not vary in space. This case is illustrated for a winter month in Figure 2b and for a summer month in Figure 3b. It is designated as the uniform rainbelt, abbreviated U_RB. Figure 1b suggests this is not as bad as an assumption as one might first guess given that the rainbelt characteristics do not exhibit strong discontinuities between land and ocean. In this case:

$$\chi(t) = \frac{\tilde{P}_\ell(t)}{\tilde{P}_o(t)}. \tag{2}$$

$\tilde{P}_\ell(t)$ and $\tilde{P}_o(t)$ denote the monthly mean tropical precipitation (mm day^{-1}) obtained from the rainbelt model, conditionally averaged over tropical land and over tropical ocean, respectively. They can be derived knowing the three parameters of the rainbelt model as

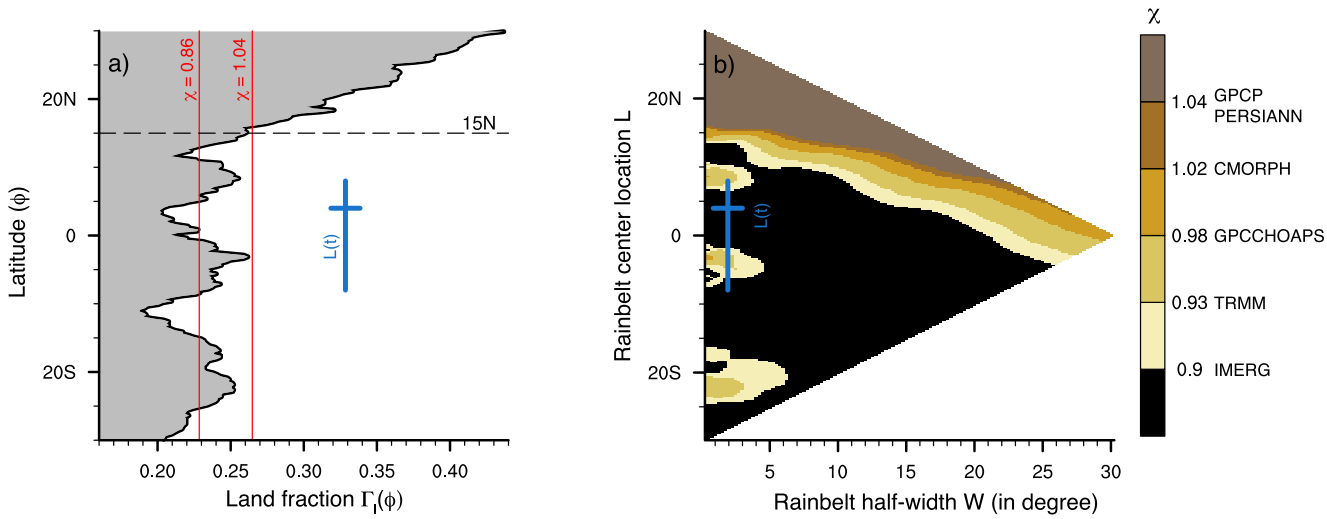

Figure 4. Constraints implied by the land-sea distribution on χ with (a) zonally averaged land fraction $\Gamma_\ell(\phi)$ and (b) theoretical estimates of χ computed using Equation 5. In panel (a), all data taken from TRMM; the vertical blue bar denotes the hydrological equator and the horizontal bar its most frequent location. The two red vertical lines show the mean land fraction averaged south of 15°N and the mean land fraction required to match the largest of the observed χ (1.04). In panel (b), color levels are chosen to match observed χ.

$$\tilde{P}_{\ell,o}(t) = \frac{I(t)\int_{-180^\circ}^{180^\circ}\int_{L(t)-W}^{L(t)+W}\Gamma_{\ell,o}(\lambda,\phi)\cos(\phi)\,d\phi\,d\lambda}{\langle\Gamma_{\ell,o}(\lambda,\phi)\rangle} \tag{3}$$

Equation 3 assumes that the intensity is zero outside of the rainbelt and that neither intensity, nor location, nor width varies zonally, in agreement with our null hypothesis. Equation 3 also assumes that the half-width does not vary in time. This assumption is motivated by the analysis presented in Figure 1b where the width of the rainbelt,

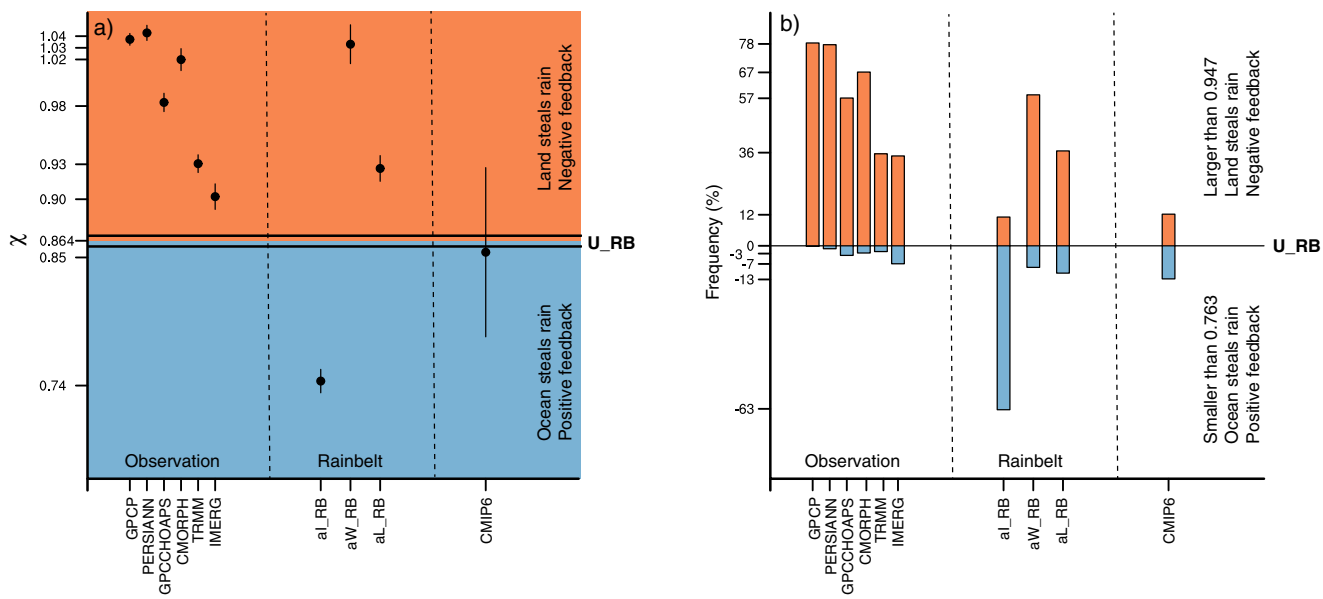

Figure 5. Statistics of $\chi(t)$ from observations (ordered by decreasing record length, see Table 1), configurations of our rainbelt model with uniform rainbelt (U_RB, Equation 5), asymmetric intensity (aI_RB, Equation 7), asymmetric width (aW_RB, Equation 9), asymmetric location (aL_RB, Equation 10), and for the CMIP6 multi model mean with (a) χ and (b) frequency of $\chi(t)$ being out of the bounds given by U_RB. Orange means that the land receives more than its fair share of precipitation, stealing some rain that ought to fall over ocean, blue that the land receives less than its fair share of precipitation. Vertical bars in panel (a) for the standard error except in CMIP6 where it represents one ensemble standard deviation. For the rainbelt models, the required input parameters are always derived from TRMM.

taken as the zonal average of the area comprised between the two white isolines, shows little seasonal variations. Inserting Equation 3 into Equation 2 gives:

$$\chi(t) = \frac{1.}{\alpha} \frac{\int_{-180°}^{180°} \int_{L(t)-W}^{L(t)+W} \Gamma_\ell(\lambda,\phi)\cos(\phi)\mathrm{d}\phi\,\mathrm{d}\lambda}{\int_{-180°}^{180°} \int_{L(t)-W}^{L(t)+W} \Gamma_o(\lambda,\phi)\cos(\phi)\,\mathrm{d}\phi\,\mathrm{d}\lambda} \tag{4}$$

or

$$\chi(t) = \frac{1.}{\alpha} \frac{\int_{L(t)-W}^{L(t)+W} \Gamma_\ell(\phi)\cos(\phi)\mathrm{d}\phi}{\int_{L(t)-W}^{L(t)+W} \Gamma_o(\phi)\cos(\phi)\,\mathrm{d}\phi} \tag{5}$$

where we drop λ from the notation in Equation 5 to denote the zonal average. Note that $\Gamma_\ell(\phi) + \Gamma_o(\phi) = 1$ and α is the known ratio between tropical land area and ocean area:

$$\alpha = \frac{\langle \Gamma_\ell(\lambda,\phi) \rangle}{\langle \Gamma_o(\lambda,\phi) \rangle} = 0.348 \tag{6}$$

The uniform rainbelt model (Equation 5) reveals that the values that $\chi(t)$ can take are constrained by the zonal extent of the land, $\Gamma_\ell(\phi)$. The latter is displayed in Figure 4a. The meridional profile indicates that the land fraction is relatively constant south of 15°N, with a mean of 0.23. Assuming thus first that the rainbelt just straddles the latitudes south of 15°N, a value of $\frac{1.}{0.348}\frac{0.23}{1-0.23} = 0.86$ is expected for χ. Hence, under the null hypothesis that the tropics-wide partitioning of precipitation is purely set by the location and size of land masses, a ratio of 0.86, not 1.0, is expected. A ratio of 1.0 would require that the land fraction that the rainbelt sees is the same as the tropics-wide land fraction, $\frac{\alpha}{1+\alpha} = 0.26$.

Second, we can contrast this expected value to observed values. Temporal averages of observed $\chi(t)$ from various data sets are displayed in Figure 5a and denoted χ. The values lie between 0.90% and 1.04%, 5%–21% larger than 0.86. To be able to explain by geometrical constraints the largest of the observed χ, 1.04 in PERSIANN, a mean land fraction of 0.27 would be required. As indicated by the second red vertical line in Figure 4a, this would require the rainbelt to often reside past 15°N. Systematically testing all potential combinations of rainbelt width and location in Figure 4b confirms that either a narrow uniform rainbelt located poleward of 15°N or, otherwise,

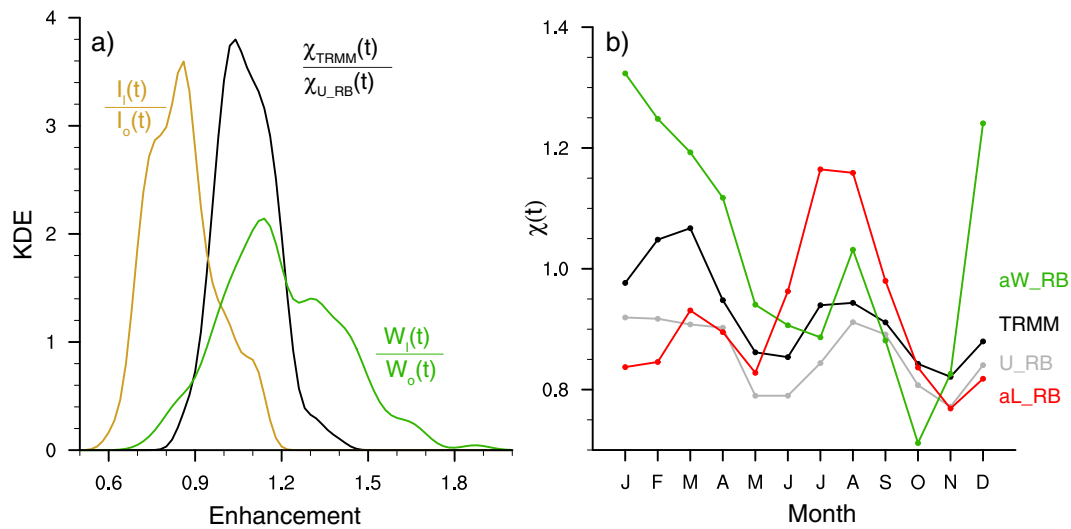

Figure 6. (a) Kernel density estimate of the enhancement of precipitation required over land to match observed $\chi(t)$ (black) compared to land enhancement resulting from intensity (brown) and width (green) changes. The Kernel density estimates were computed with NCL 6.5.0 and its built-in function using a Gaussian kernel and a bin size of 0.02 following Engel et al. (1994). Using Kernel density estimates leads to smoother curves than using histograms. Panel (b) shows the mean seasonal cycle in $\chi(t)$ from observations and from our rainbelt model with uniform rainbelt (U_RB, Equation 5), asymmetric width (aW_RB, Equation 9), and asymmetric location (aL_RB, Equation 10). Required observations taken from TRMM.

a wide enough rainbelt is needed to explain the observed χ. Both allow the rainbelt to see the larger land fraction poleward of 15°N. Both are nevertheless unlikely. Figure 1b already revealed the narrowness of the rainbelt in observations. Moreover, the monthly mean zonal averages of the observed hydrological equator, indicated by the blue bar in Figure 4a and taken as the expected observed locations $L(t)$ of the rainbelt, never lie poleward of 15°N.

As a final check, we recompute the distribution of $\chi(t)$ using now monthly mean and zonally averaged values of observed rainbelt half-width W and location $L(t)$ as input for our rainbelt model (Equation 5). W is set to 1.9°, in agreement with Figure 1b, and $L(t)$ is derived by zonally averaging the hydrological equator. The results are displayed in Figure 5a by the horizontal lines. Not surprisingly, a mean value of 0.86 is obtained, which is robustly lower than any of the observed values.

Using these observed values of rainbelt half-width W and location $L(t)$ as input for the rainbelt model also indicates that the probability distribution function of $\chi(t)$ lies between the two values of 0.76 and 0.95. These extrema are geometrically constrained by the extrema of the land fraction (see Figure 4a) and the rainbelt width, as given by Equation 5. Figure 5b indicates how often observed values of $\chi(t)$ lie outside these bounds. Whereas the lower bound is roughly consistent with the data, observed values exceed the upper bound 35% (IMERG) to 78% (GPCP) of the time, that is, for 4–9 months per year.

5. Land Overcompensates Its Geometrical Deficit by Making the Rainbelt Wider and Letting It Move More

Our conceptual model refutes the null hypothesis and indicates that the land receives more than its fair share of precipitation. How is the geometrical deficit of the land overcompensated? Given that storms are more explosive over land (Bang & Zipser, 2015), one answer could be that the anomalous precipitation over land arises from asymmetries in intensity between land and ocean. Figure 6a quantifies how much the intensity in our rainbelt model needs to be enhanced over land to explain the observed $\chi(t)$ (black curve) and compares this enhancement to observed ratios of intensity between land and ocean (brown curve). The intensity $I(\lambda, t)$ is defined for each longitude and month as the observed monthly mean precipitation rate at the location of the meridional precipitation maximum (the hydrological equator), motivated by the results of Figure 1, and conditionally averaged over land (I_ℓ) and over ocean (I_o) precipitation maxima. Using other definitions, such as mean precipitation larger than a certain threshold or precipitation averaged over a certain area, would confound effects resulting from intensity, width, and rainbelt movement.

Figure 6a indicates that asymmetric intensities cannot explain the observed values of χ being larger than 0.86. I_ℓ is actually smaller than I_o (see also Figure 1b) with a value of 14.6 versus 17.2 mm day^{-1} in observations. This hypothesis of asymmetric intensities can be further tested by allowing for asymmetric intensities between land and ocean in our rainbelt model, effectively replacing $I(t)$ by $I_{\ell,o}(t)$ in Equation 3. This leads to:

$$\chi(t) = \frac{1.}{\alpha}\frac{I_\ell(t)}{I_o(t)}\frac{\int_{L(t)-W}^{L(t)+W}\Gamma_\ell(\phi)\cos(\phi)\mathrm{d}\phi}{\int_{L(t)-W}^{L(t)+W}\Gamma_o(\phi)\cos(\phi)\,\mathrm{d}\phi}. \tag{7}$$

The result of evaluating Equation 7 is displayed in Figure 5a as the asymmetric intensity rainbelt, aI_RB, now using observed values of $I_\ell(t)$, $I_o(t)$, $L(t)$ and W as input. Allowing for distinct intensities over land and ocean lowers χ to 0.74, further away from observations.

In contrast, letting the rainbelt width over ocean and land be different (see green curve in Figure 6a) reveals larger (~20%) width over land in observations. The needed half-width values $W(\lambda, t)$ are here computed for every longitude and month as:

$$W(\lambda,t) \equiv \frac{\phi_2(\lambda,t) - \phi_1(\lambda,t)}{2.} \tag{8}$$

where ϕ_2 and ϕ_1 correspond to the first latitudes north and south of the hydrological equator where the precipitation drops to a fraction C of its value at the hydrological equator. If this condition is not met inside the tropics, then 30° is used for the corresponding bound. In mathematical terms: $P(\lambda, \phi, t) > C \cdot P(\lambda, L, t)\ \forall\ \phi \in [\phi_1, \phi_2]$ and $\|\phi\| \leq 30°$. We use $C = 0.5$ based on the results of Figure 1b. The half-width values are then conditionally

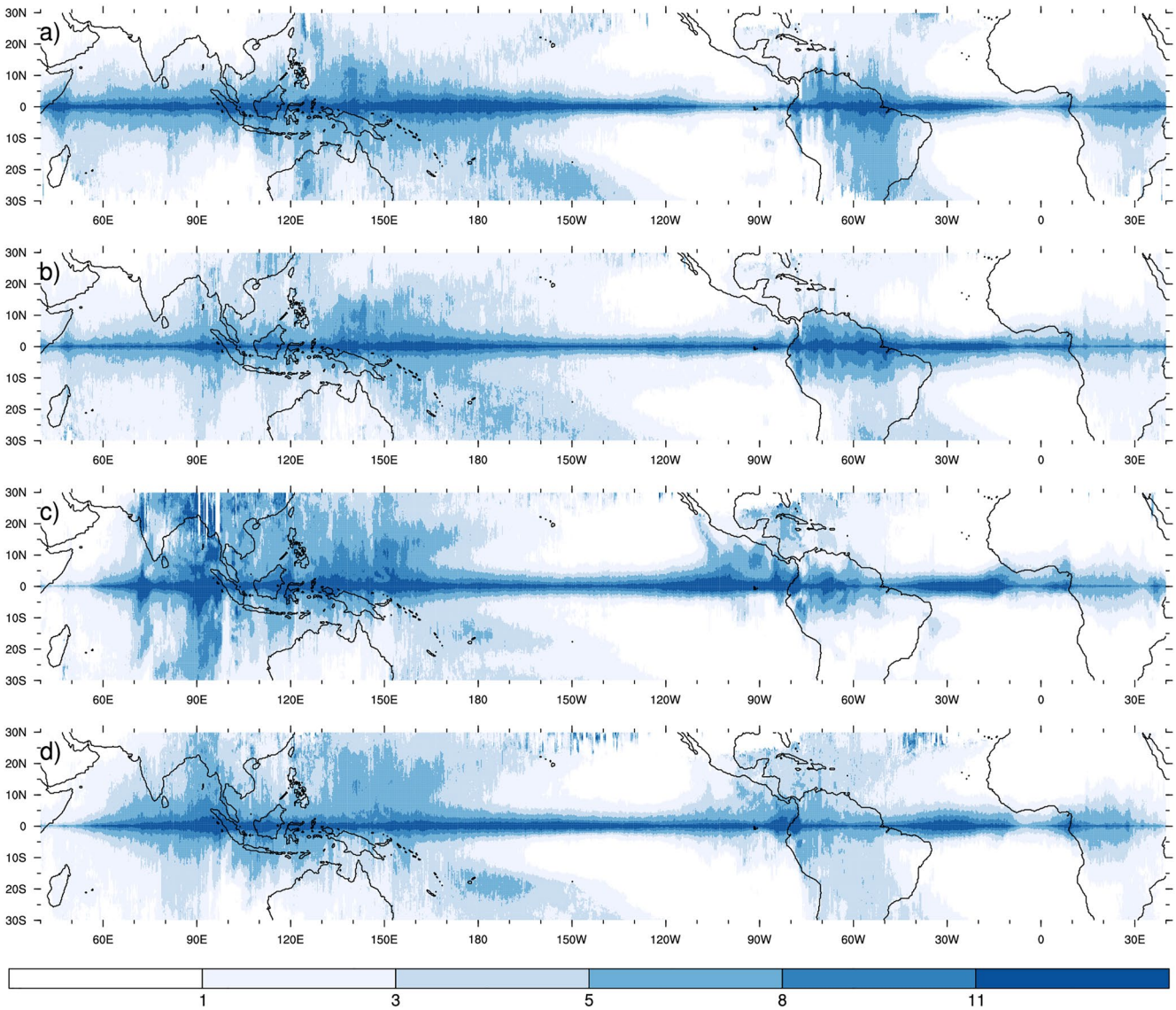

Figure 7. As Figure 1b, but averaged over (a) DJF, (b) MAM, (c) JJA, and (d) SON.

averaged over land (W_ℓ) and ocean (W_o) using $L(\lambda, t)$ to distinguish between land and ocean points. This is an approximation, as in coastal areas the points enclosed by $W(\lambda, t)$ would belong both to the ocean and to the land. This approximation nevertheless does not affect the overall results.

As shown in Figure 6a, the enhancement due to asymmetric width is strong enough to compensate for the land deficit. This is further demonstrated by recomputing $\chi(t)$ solely allowing for asymmetric width between land and ocean in our rainbelt model, a configuration visualized in Figures 2c and 3c for a winter and a summer month. In this case, $\chi(t)$ equals:

$$\chi(t) = \frac{1.}{\alpha} \frac{\int_{L(t)-W_\ell(t)}^{L(t)+W_\ell(t)} \Gamma_\ell(\phi)\cos(\phi)\mathrm{d}\phi}{\int_{L(t)-W_o(t)}^{L(t)+W_o(t)} \Gamma_o(\phi)\cos(\phi)\,\mathrm{d}\phi}. \tag{9}$$

Note that Equation 9, in contrast to the uniform rainbelt model in Equation 5, retains the temporal variations in width as those are large over land, as can be seen by comparing Figures 2c and 3c. Equation 9 is then again evaluated using observations as input and the results are summarized in Figure 5 as the asymmetric width rainbelt, aW_RB. Equation 9 leads to a mean χ of 1.03. More importantly, $\chi(t)$ being larger than 0.95, the upper bound

of possible values in the uniform case, now happens 58% of the time. Both characteristics are comparable to observations.

But the rainbelt also sporadically visits locations poleward of 15°N in observations, a feature associated with the Asian monsoon (see Figure 3a). These land points are not seen in the uniform rainbelt model when using the observed zonally averaged hydrological equator as input for $L(t)$ since only a small fraction of these locations, at most 7% for a given month, lies poleward of 15°N. We thus allow the rainbelt in our model to wander following $L(\lambda, t)$, see Figures 2d and 3d. This is a more extreme case than just allowing two different values for $L_\ell(t)$ and $L_o(t)$ over land and over ocean, as done for the intensity and width. We do so especially to allow the rainbelt model to see land points poleward of 15°N in summer. Recomputing $\chi(t)$ by replacing $L(t)$ by $L(\lambda, t)$ in Equation 4 leads to:

$$\chi(t) = \frac{1.}{\alpha} \frac{\int_{-180°}^{180°} \int_{L(\lambda,t)-W}^{L(\lambda,t)+W} \Gamma_\ell(\lambda,\phi)\cos(\phi)\mathrm{d}\phi\,\mathrm{d}\lambda}{\int_{-180°}^{180°} \int_{L(\lambda,t)-W}^{L(\lambda,t)+W} \Gamma_o(\lambda,\phi)\cos(\phi)\,\mathrm{d}\phi\,\mathrm{d}\lambda} \tag{10}$$

The case is denoted as the asymmetric location rainbelt, aL_RB, and the obtained $\chi(t)$ values from Equation 10 are summarized in Figure 5. As expected, the frequency of $\chi(t)$ values larger than 0.95 increases and χ also increases in comparison to the uniform case, leading to a better agreement with observations.

The fact that the land broadens the rainbelt more and moves it more makes the continents rainier than expected from geometrical constraints. Considering the seasonal cycle of $\chi(t)$ in Figure 6b reveals a distinct seasonality in these two processes. This distinct seasonality is also well visible when comparing the spatial rendering of our rainbelt model configurations for a winter (Figure 2) and summer (Figure 3) month. The asymmetric width is needed to explain the observed enhancement of $\chi(t)$ during boreal winter, although the rainbelt model (aW_RB) overinflates this peak. In contrast, allowing for asymmetric locations in aL_RB only affects simulated boreal summer values and strongly overestimates those as compared to observations. This overestimation illustrates a limitation of our rainbelt model: aL_RB retains mostly the maxima associated with the Asian monsoon (see Figure 3a), whereas in observations, secondary maxima appear over the Indian Ocean. Hence, our assumption of one single rainbelt partly breaks down in boreal summer, as also visible in Figure 7 when averaging the shifted precipitation distribution per season. This limitation of our rainbelt model may also illustrate that there is a limit in reality as to how strongly the geometrical deficit of the land can be compensated by attracting precipitation poleward in regions of much higher land fraction, as anomalously poleward displacements of the rainbelt over land can be compensated by the emergence of secondary bands of precipitation over ocean.

6. Summary and Discussion

Overall, our conceptualization of the distribution of tropical precipitation in the form of a rainbelt model indicates that the land receives more than its fair share of precipitation as set by the size and location of land masses: all the observational data sets reveal a tropical land-to-ocean precipitation ratio larger than 0.86. In the uniform rainbelt model, not distinguishing between land and ocean controls on the atmospheric properties implies that the mean evapotranspiration averaged over the land points equals the mean evaporation averaged over the ocean points. It is thus larger than the evapotranspiration averaged over a true land surface. But at the same time, the land points in the uniform rainbelt model receive in mean less precipitation than over a true land surface, given the smaller χ and assuming the same tropics-wide mean precipitation. In summary, implicitly putting land to ocean in the uniform rainbelt model leads to an increased evapotranspiration and decreased precipitation compared to a true land surface, a finding that we interpret as being indicative of the existence of a negative feedback between evapotranspiration and precipitation. A negative feedback is needed to explain the long-term tropics-wide partitioning of precipitation between land and ocean and, on a monthly basis, the negative feedback dominates. This finding seems at odds with climate models which predominantly simulate a positive feedback between evapotranspiration and precipitation in response to land surface perturbations, such as an increase in soil moisture. Are climate models thus misrepresenting the feedback, here deduced in a distinct way by quantifying the strength of the land control on the tropics-wide partitioning of precipitation? Looking at χ in the CMIP6 multi model mean in Figure 5a reveals a value of 0.85, too low compared to observations, and even indicative of a slight tendency of the land to receive less than its fair share of precipitation, that is, to lose some precipitation to the ocean. More

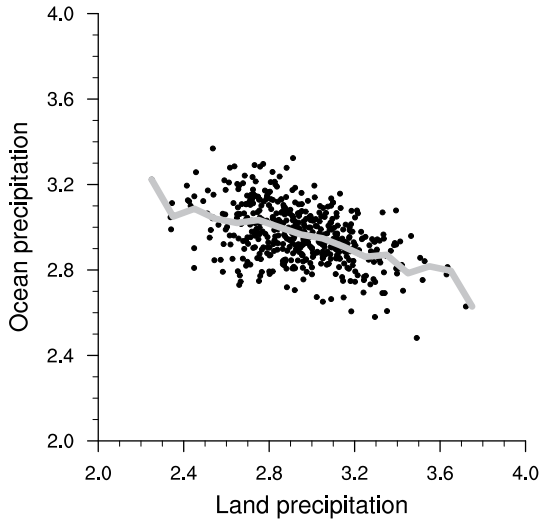

Figure 8. Scatterplot of monthly mean values of precipitation averaged over tropical land points only and over tropical ocean points. The gray line shows the ocean precipitation binned by the land precipitation; it would match the regression line ($y = 3.75 - 0.27x$, $R2 = 0.22$). All values in mm day^{-1} and taken from the long GPCP record.

strikingly, on a monthly basis, ocean and land steal from each other rain as frequently, whereas it should be at most one out of nine cases (see IMERG in Figure 5b) that the land receives less than its fair share of precipitation. Twenty two of the 39 CMIP6 models do indicate that the land receives more than its fair share of precipitation, albeit with a too weak magnitude, and most (18) for the wrong reason, by having I_ℓ larger than I_o. The 17 CMIP6 models where land receives less than its fair share of precipitation do so for two reasons. First, only four of these models capture the expected width enhancement over land and eight of the 17 actually have W_ℓ smaller than W_o. Second, too often the hydrological equator falls over ocean instead of land. This can be seen by using the hydrological equator derived for each individual CMIP6 model as input for $L(\lambda, t)$ in the asymmetric location rainbelt aL_RB. For the 17 CMIP6 models where land receives less than its fair share of precipitation, this analysis reveals that 13 of them have a χ smaller than 0.93, the value obtained for aL_RB using observations as input. Except in one model, which strongly underestimates I_ℓ as compared to I_o, intensity cannot be invoked to explain the failure of CMIP6 models to capture precipitation enhancement over land. The fact that climate models cannot represent the effect of a perturbation of the surface characteristics, from ocean to land, on a basic property of the precipitation distribution, its partitioning, calls into question the ability of climate models to answer more subtle questions like future tropical regional precipitation changes. The results also suggest that the land may be more resilient to perturbations than models might have led us to believe, with the land being less dependent on its own water supply and hence more resilient to the occurrence of tipping points.

Our study demonstrates the power of geometrical constraints to explain basic features of the precipitation distribution and the potential usefulness of considering the precipitation ratio, rather than precipitation amounts per se. The use of $\chi(t)$ is best justified taking the view that the precipitation averaged over the whole tropics is set and land and ocean have to compete for this given resource. We cannot demonstrate this assumption at the outset, but we note that it is broadly consistent with the fact that monthly mean precipitation amounts over land and over ocean are negatively correlated (see Figure 8). A potential explanation could be that stronger ascent over land (more precipitation) has to be compensated by stronger subsidence over ocean (less precipitation), assuming that the export of water to the extratropics is held fixed.

The findings of our study are conditioned on the ability of our rainbelt model to capture the precipitation dynamics to a first order. Correlation between $\chi(t)$ derived from TRMM and from our simplest conceptualization, the uniform rainbelt model, is surprisingly high, 0.55, compared to 0.45 for the CMIP6 multi model mean. Also, the seasonal cycle in $\chi(t)$ is very well reproduced, albeit being shifted to lower values (see Figure 6b). The findings are also robust to the chosen definition of the tropics and to the observational data set chosen to derive the input parameters of the rainbelt model. The only noteworthy sensitivity is in the case of the asymmetric location (aL_RB). All the data sets show an increased occurrence of $\chi(t)$ being larger than 0.95. All the data sets except IMERG also lead to an increase of χ as compared to the uniform case (U_RB). With IMERG, χ does not change. We also tested the sensitivity of the results to the definition of the rainbelt width, of relevance for the asymmetric width rainbelt (aW_RB). Using a more stringent threshold of 75% to define $W(\lambda, t)$ reduces χ to 0.95 and the frequency of $\chi(t)$ values larger than 0.95%–36%, compared to a χ of 1.03 and a frequency of 58% when using a threshold of 50%. This is expected from the land-sea distribution, where the mere presence of a wider belt tends to help the land, as seen in Figure 4b.

The results of our study are only valid for the given land-sea distribution. Changing the location or size of land masses would affect the precipitation distribution (Dirmeyer, 1998; Xie & Saito, 2001) and its propensity to be represented by a rainbelt. Also, although we demonstrated that the land receives more than its fair share of precipitation by having a wider rainbelt and moving it more, and not via changes in intensity, it especially remains an open question why the width is larger over land. Recent studies based on idealized frameworks (Hohenegger & Stevens, 2018; Leutwyler & Hohenegger, 2020) and/or looking at other properties of the climate

system (Byrne, 2021) have argued that the limited water availability of the land is a decisive property for making land distinct from ocean. Other suspects could be its stronger heterogeneity and roughness or a smaller effective surface heat capacity, the latter known to be important for the propagation of the monsoons (Halley, 1686). Mountains could also affect $\chi(t)$, but their expected direct effect would be via an increased precipitation intensity or by violating the rainbelt assumption, both of which we can rule out from our analysis. Studies have begun exploring theoretical frameworks to understand the processes that set the width of the zonally averaged tropical rainbelt (see Windmiller and Hohenegger (2019) and review by Byrne et al. (2018)), but these studies haven't yet attempted to explain differences observed between land and ocean.

In our interpretation of the precipitation behavior over the tropics with our conceptual model, the fact that the land supports a wider rainbelt and moves it more leads to the existence of a negative feedback between precipitation and evapotranspiration. Scheff (2014) showed that including ocean heat transport in simulations with an idealized representation of continents leads to an enhancement of precipitation over land. We nevertheless note that in his simulations, evapotranspiration increases as well, unlike in our findings. Precipitation and evaporation are connected via the water balance equation. The land, in contrast to the ocean, continuously loses water due to runoff. This implies that, over land, the ratio between precipitation and evaporation has to be larger than over ocean. This nevertheless also does not provide any constraint on the sign of precipitation changes, $P_\ell - P_o$, versus evapotranspiration changes, $E_\ell - E_o$. More importantly, our study indicates that the magnitude of $\chi(t)$, being larger or smaller than 0.86, can be used as an indicator of the sign of the feedback between precipitation and evapotranspiration. Given that most of the observational spread in $\chi(t)$ comes from uncertain precipitation amounts over ocean, better understanding precipitation over land and its constraints will especially require a better ability to measure precipitation amounts over ocean.

Conflict of Interest

The authors declare no conflict of interest relevant to this study.

Data Availability Statement

The material (manuscript text, code, and scripts used to produce the figures) can be accessed at: http://hdl.handle.net/21.11116/0000-000A-1DEC-D. All data are freely available from the internet. The output of the CMIP6 models can be downloaded here: https://esgf-data.dkrz.de/search/cmip6-dkrz/. The observational data sets were obtained from: https://icdc.cen.uni-hamburg.de for GPCP, GPCC and HOAPS; https://chrsdata.eng.uci.edu/ for PERSIANN-CDR; https://gpm.nasa.gov/data/directory for IMERG; https://disc.gsfc.nasa.gov/datasets/ for TRMM and https://climatedataguide.ucar.edu/climate-data/ for CMORPH. GPCP and CMORPH are provided by the NOAA, GPCC by the DWD, HOAPS by the EUMETSAT, and TRMM and IMERG by the NASA/Goddard Space Flight Center.

Acknowledgments
The authors would like to thank Victor Brovkin for comments on an earlier version of the manuscript, the two reviewers Mike Byrne and Jack Scheff for their constructive and insightful comments, the CMIP community for providing the climate simulations, and the mission scientists and associated personnel for the production of the observational data. Open Access funding enabled and organized by Projekt DEAL.

References

Adler, R., Wang, J.-J., Sapiano, M., Huffman, G., Chiu, L., Xie, P., et al. (2016). *Global Precipitation Climatology Project (GPCP) climate data record (CDR), version 2.3 (monthly)*. National Centers for Environmental Information. https://doi.org/10.7289/V56971M6

Andersson, A., Graw, K., Schröder, M., Fennig, K., Liman, J., Bakan, S., et al. (2017). Hamburg ocean atmosphere parameters and fluxes from satellite data – HOAPS 4.0. Satellite application facility on climate monitoring. https://doi.org/10.5676/EUM_SAF_CM/HOAPS/V002

Ashouri, H., Hsu, K. L., Sorooshian, S., Braithwaite, D. K., Knapp, K. R., Cecil, L. D., et al. (2015). PERSIANN-CDR: Daily precipitation climate data record from multisatellite observations for hydrological and climate studies. *Bulletin America Meteorology Social*, *96*(1), 69–83. https://doi.org/10.1175/BAMS-D-13-00068.1

Bang, S. D., & Zipser, E. J. (2015). Differences in size spectra of electrified storms over land and ocean. *Geophysical Research Letters*, *42*(16), 6844–6851. https://doi.org/10.1002/2015gl065264

Bordoni, S., & Schneider, T. (2008). Monsoons as eddy-mediated regime transitions of the tropical overturning circulation. *Nature Geoscience*, *1*(8), 515–519. https://doi.org/10.1038/ngeo248

Byrne, M. (2021). Amplified warming of extreme temperatures over tropical land. *Nature Geoscience*, *14*(11), 837–841. https://doi.org/10.1038/s41561-021-00828-8

Byrne, M., Pendergrass, A. G., Rapp, A. D., & Wodzicki, K. R. (2018). Response of the intertropical convergence zone to climate change: Location, width, and strength. *Current Climate Change Reports*, *4*, 355–370. https://doi.org/10.1007/s40641-018-0110-5

Dirmeyer, P. A. (1998). Land-sea geometry and its effect on monsoon circulations. *Journal of Geophysical Research*, *103*(D10), 11555–11572. https://doi.org/10.1029/98jd00802

Engel, J., Herrmann, E., & Gasser, T. (1994). An iterative bandwidth selector for kernel estimation of densities and their derivatives. *Journal of Nonparametric Statistics*, *4*(1), 21–34. https://doi.org/10.1080/10485259408832598

Fiedler, S., Crueger, T., D'Agostino, R., Peters, K., Becker, T., Leutwyler, D., et al. (2020). Simulated tropical precipitation assessed across three phases of the Coupled Model Intercomparison Project (CMIP). *Monthly Weather Review*, *148*(9), 3653–3680. https://doi.org/10.1175/mwr-d-19-0404.1

Frierson, D. M. W., Hwang, Y.-T., Fuckar, N. S., Seager, R., Kang, S. M., Donohoe, A., et al. (2013). Contribution of ocean overturning circulation to tropical rainfall peak in the northern hemisphere. *Nature Geoscience*, *6*(11), 940–944. https://doi.org/10.1038/ngeo1987

Gray, W. M., & Jacobson, R. W. (1977). Diurnal variation of deep convection. *Monthly Weather Review*, *105*(9), 1171–1188. https://doi.org/10.1175/1520-0493(1977)105<1171:dvodcc>2.0.co;2

Halley, E. (1686). An historical account of the trade winds and monsoons, observable in the seas between and near the tropics, with an attempt to assign the physical cause of the said winds. *Philosophical Transactions of the Roy. Society*, *16*(183), 153–168. https://doi.org/10.1098/rstl.1686.0026

Hohenegger, C., Brockhaus, P., Bretherton, C. S., & Schär, C. (2009). The soil-moisture precipitation feedback in simulations with explicit and parameterized convection. *Journal of Climate*, *22*(19), 5003–5020. https://doi.org/10.1175/2009jcli2604.1

Hohenegger, C., & Stevens, B. (2018). The role of the permanent wilting point in controlling the spatial distribution of precipitation. *Proceedings of the National Academy of Sciences*, *115*(22), 5692–5697. https://doi.org/10.1073/pnas.1718842115

Huffman, G. J., Bolvin, D. T., Nelkin, E. J., & Adler, R. F. (2016). *TRMM (TMPA) Precipitation L31 day 0.25 degree x 0.25 degree V7* (In A. Savtchenko (Ed.). Goddard Earth Sciences Data and Information Services Center (GES DISC). https://doi.org/10.5067/TRMM/TMPA/DAY/7

Huffman, G. J., Bolvin, D. T., Nelkin, E. J., Stocker, E. F., & Tan, J. (2020). V06 IMERG release notes. Technical documentation. https://docserver.gesdisc.eosdis.nasa.gov/public/project/GPM/IMERG_V06_release_notes.pfd

Huffman, G. J., Stocker, E. F., Bolvin, D. T., Nelkin, E. J., & Tan, J. (2019). *GPM IMERG final precipitation L31 month 0.1 degree x 0.1 degree V06*. Goddard Earth Sciences Data and Information Services Center (GES DISC). https://doi.org/10.5067/GPM/IMERG/3B-MONTH/06

Joyce, R. J., Janowiak, J. E., Arkin, P. A., & Xie, P. (2004). CMORPH: A method that produces global precipitation estimates from passive microwave and infrared data at high spatial and temporal resolution. *Journal of Hydrometeorology*, *5*(3), 487–503. https://doi.org/10.1175/1525-7541(2004)005<0487:camtpg>2.0.co;2

Kang, S. M., Held, I. M., Frierson, D. M. W., & Zhao, M. (2008). The response of the ITCZ to extratropical thermal forcing: Idealized slab-ocean experiments with a GCM. *Journal of Climate*, *21*(14), 3521–3532. https://doi.org/10.1175/2007jcli2146.1

Koster, R. D., Dirmeyer, P. A., Guo, Z., Bonan, G., Chan, E., Cox, P., et al. (2004). Regions of strong coupling between soil moisture and precipitation. *Science*, *305*(5687), 1138–1140. https://doi.org/10.1126/science.1100217

Leutwyler, D., & Hohenegger, C. (2020). Weak cooling of the troposphere by tropical islands in simulations of the radiative-convective equilibrium. *Quarterly Journal of the Royal Meteorological Society*, *147*(736), 1788–1800. https://doi.org/10.1002/qj.3995

Philander, S. G. H., Gu, D., Halpern, D., Lambert, G., Lau, N.-C., Li, T., & Pacanowski, R. C. (1996). Why the ITCZ is mostly north of the equator. *Journal of Climate*, *9*(12), 2958–2972. https://doi.org/10.1175/1520-0442(1996)009<2958:wtiimn>2.0.co;2

Pielke, R. A. (2001). Influence of the spatial distribution of vegetation and soils on the prediction of cumulus convective rainfall. *Reviews of Geophysics*, *39*(2), 151–177. https://doi.org/10.1029/1999rg000072

Rhea, J. O. (1966). A study of thunderstorm formation along dry lines. *Journal of Applied Meteorology*, *12*, 546–547. https://doi.org/10.1175/1520-0450(1966)005<0058:ASOTFA>2.0.CO;2

Riehl, H. (1954). *Tropical meteorology* (p. 392). McGraw-Hill.

Roe, G. H. (2005). Orographic precipitation. *Annual Review of Earth and Planetary Sciences*, *33*(1), 645–671. https://doi.org/10.1146/annurev.earth.33.092203.122541

Scheff, J. (2014). *Understanding the responses of precipitation, evaporative demand, and terrestrial water availability to planetary temperature in climate models* (PhD dissertation). University of Washington.

Schneider, U., Becker, A., Finger, P., Meyer-Christoffer, A., & Ziese, M. (2018). GPCC monitoring product: Near real-time monthly land-surface precipitation from rain-gauges based on SYNOP and CLIMAT data. https://doi.org/10.5676/DWD_GPCC/MP_M_V6_100

Sobel, A. H., Burleyson, C. D., & Yuter, S. E. (2011). Rain on small tropical islands. *Journal of Geophysical Research*, *116*(D8), D08102. https://doi.org/10.1029/2010jd014695

Sun, Q., Miao, C., Duan, Q., Ashouri, H., Sorooshian, S., & Hsu, K.-L. (2018). A review of global precipitation datasets: Data sources, estimation, and intercomparisons. *Reviews of Geophysics*, *56*(1), 2017RG000574. https://doi.org/10.1002/2017rg000574

Taylor, C. M., Birch, C. E., Parker, D. J., Dixon, N., Guichard, F., Nikulin, G., & Lister, G. M. S. (2013). Modeling soil moisture-precipitation feedback in the Sahel: Importance of spatial scale versus convective parameterization. *Geophysical Research Letters*, *40*(23), 2013GL058511. https://doi.org/10.1002/2013gl058511

Taylor, C. M., Gounou, A. M., Guichard, F., Harris, P. P., Ellis, R. J., Couvreux, F., & de Kauwe, M. (2011). Frequency of Sahelian storm initiation enhanced over mesoscale soil-moisture patterns. *Nature Geoscience*, *4*(7), 430–433. https://doi.org/10.1038/ngeo1173

Wallace, J. M. (1975). Diurnal variations in precipitation and thunderstorm frequency over the conterminous United States. *Monthly Weather Review*, *103*(5), 406–419. https://doi.org/10.1175/1520-0493(1975)103<0406:dvipat>2.0.co;2

Windmiller, J., & Hohenegger, C. (2019). Convection on the edge. *Journal of Advances in Modeling Earth Systems*, *11*(12), 3959–3972. https://doi.org/10.1029/2019ms001820

Xie, S.-P., & Saito, K. (2001). Formation and variability of a northerly ITCZ in a hybrid coupled AGCM: Continental forcing and oceanic-atmospheric feedback. *Journal of Climate*, *14*(6), 1262–1276. https://doi.org/10.1175/1520-0442(2001)014<1262:favoan>2.0.co;2

Zipser, E. J., & LeMone, M. A. (1980). Cumulonimbus vertical velocity events in GATE. Part II: Synthesis and model core structure. *Journal of the Atmospheric Sciences*, *37*(11), 2458–2469. https://doi.org/10.1175/1520-0469(1980)037<2458:cvveig>2.0.co;2